

# Cryogenic Terahertz Spectrum of (+)-Methamphetamine Hydrochloride and Assignment Using Solid-State Density Functional Theory

Patrick M. Hakey,<sup>†</sup> Damian G. Allis,<sup>†,‡</sup> Wayne Ouellette,<sup>†</sup> and Timothy M. Korter\*,<sup>†</sup>

Department of Chemistry, Syracuse University, Syracuse, New York 13244-4100, and Nanorex, Inc., P.O. Box 7188, Bloomfield Hills, Michigan 48302-7188

Received: November 21, 2008; Revised Manuscript Received: March 2, 2009

The cryogenic terahertz spectrum of (+)-methamphetamine hydrochloride from 10.0 to 100.0 cm<sup>-1</sup> is presented, as is the complete structural analysis and vibrational assignment of the compound using solid-state density functional theory. This cryogenic investigation reveals multiple spectral features that were not previously reported in room-temperature terahertz studies of the title compound. Modeling of the compound employed eight density functionals utilizing both solid-state and isolated-molecule methods. The results clearly indicate the necessity of solid-state simulations for the accurate assignment of solid-state THz spectra. Assignment of the observed spectral features to specific atomic motions is based on the BP density functional, which provided the best-fit solid-state simulation of the experimental spectrum. The seven experimental spectral features are the result of thirteen infrared-active vibrational modes predicted at a BP/DNP level of theory with more than 90% of the total spectral intensity associated with external crystal vibrations.

## I. Introduction

Terahertz (THz, far-infrared, <200 cm<sup>-1</sup>) vibrational spectroscopy has found use in numerous fields, including threat detection<sup>1–3</sup> and pharmaceutical characterization.<sup>4,5</sup> Its utility stems from solid-state compounds and molecules containing low-energy vibrations that, taken as a whole in this region, serve as spectral “fingerprints” that are usable for their identification, detection, and characterization. In all cases, the use of these fingerprints is dependent on the level of confidence that exists in the understanding of the molecular origins of the spectral features. The identification of these motions plays a key role in properly interpreting the features that are present in experimental spectra, making identification a critical step in the rational use of THz spectroscopy in all analytical applications.

Whereas there is a significant body of literature on the THz spectroscopy of pharmaceuticals, there has been relatively little work done on the use of THz spectroscopy for the detection and identification of concealed illicit drugs.<sup>6–8</sup> The investigation presented here is of the compound *N*-methyl-1-phenylpropan-2-aminium chloride, C<sub>10</sub>H<sub>16</sub>N•Cl, more commonly known as (+)-methamphetamine hydrochloride (METH.HCl). The compound is a potent synthetic sympathomimetic drug and a commonly abused stimulant and is listed as a schedule II controlled substance by the United States Federal government.<sup>9</sup> The popularity of methamphetamine is tied to its stimulant effects, which are comparable to the effects provided by the use of cocaine, but with longer duration.<sup>10</sup> Two enantiomers of the compound are available, with the dextrorotatory (+) enantiomer exhibiting effects roughly five times more powerful than those of the levorotatory (−) enantiomer.<sup>10</sup> The substantial potency of methamphetamine, along with its synthetic access to illicit users,<sup>11</sup> plays important roles in defining its scientific interest as a target for THz investigation.

In this work, we present the experimental THz spectra (0.3–3.0 THz, 10.0–100.0 cm<sup>-1</sup>) of METH.HCl at room (294 K) and liquid-nitrogen (78.4 K) temperatures as well as the complete first-principles analysis and assignment of the spectra using solid-state density functional theory (DFT). The room temperature THz spectrum of METH.HCl has been the subject of several previous investigations,<sup>12–14</sup> including Li et al. (2005)<sup>12</sup> and Kanamori et al. (2005),<sup>13</sup> which provide spectra over the range of frequencies from 0.2 to 2.6 THz (6.7 to 86.7 cm<sup>-1</sup>) and 0.6 to 3.0 THz (20.0 to 100.0 cm<sup>-1</sup>), respectively. In these spectra, a total of four spectral absorptions were noted, with a fifth possible feature reported in the latter investigation. The cryogenic investigation in this study provides a more feature-rich experimental spectrum than the previous room-temperature data. Through cooling, two additional spectral features are identified, bringing the total number of observed features in the METH.HCl THz spectrum to seven.

## II. Methods

**A. Experimental.** Experimental spectra were recorded using a pulsed time-domain THz spectrometer. Optical rectification is used to generate THz radiation, whereas free-space electro-optic sampling (FSEOS) is employed to detect the generated THz pulses.

A regeneratively amplified mode-locked Ti/sapphire (Ti/S) laser system comprised of four components is the foundation of the THz-TDS instrument. A diode-pumped solid-state (Nd/YVO<sub>4</sub>) laser (Coherent, Verdi-5) is used to pump a Ti/S oscillator (Coherent, Mira-SPO), which seeds a Ti/S regenerative amplifier (Positive Light, Legend-HE-USP). A second diode-pumped solid-state (Nd/YLF) laser (Positive Light, Evolution-30) serves to pump the regenerative amplifier. Overall, this system delivers ultrashort pulses at a 1 kHz repetition rate with a duration of ≤40 fs and energy of ~2.5 mJ centered at  $\lambda = 800$  nm. The near-infrared (NIR) pulses then propagate through a 0.5 mm zinc telluride generator crystal, creating the THz radiation via the second-order nonlinear optical process of optical rectification.<sup>15,16</sup> Ultimately, this system generates THz

\* Corresponding author. E-mail: tmkorter@syr.edu.

<sup>†</sup> Syracuse University.

<sup>‡</sup> Nanorex, Inc.

pulses with a bandwidth of 10.0–100.0 cm<sup>-1</sup> and duration of ~200 fs. Any residual NIR radiation is eliminated by the presence of a polytetrafluoroethylene (PTFE) disk directly behind the generator crystal. The THz radiation is directed and focused toward the sample via a pair of off-axis parabolic mirrors.

The sample is held in an evacuated variable-temperature cryostat (Janis Research Systems) to allow for temperature studies. The cryostat windows are composed of polymethylpentene (3 mm) because of its low absorbance of THz radiation and high rigidity. In the studies presented here, the cryostat is maintained at 294 and 78.4 K, corresponding to room temperature and liquid-nitrogen temperatures, respectively. To negate the effects of ambient water vapor, the entire path of the THz pulses is purged with dry air.

After interacting with the sample pellet, the transmitted THz radiation is focused on a second ZnTe crystal (0.5 mm) by a second pair of off-axis parabolic mirrors. This crystal serves as the detector in the FSEOS method<sup>17</sup> where the THz pulses induce a birefringence within the ZnTe crystal that is directly proportional to the amplitude and phase of the electric field of the THz pulse. We measured the induced birefringence by monitoring the amount of polarization rotation in an NIR gate pulse that spatially and temporally overlaps the THz pulse in the ZnTe crystal. A Wallaston prism and a balanced photoreceiver (New Focus 2307) are used with a lock-in amplifier (Stanford SR-830) to monitor the polarization of the NIR gate pulse. The amplifier is locked to an optical chopper (Digirad C-980) inserted into the THz generation arm, and itself is synchronized with a subharmonic of the laser-repetition rate. A linear delay stage (Newport ILS150CCHA) is used to vary the arrival time of the THz pulses relative to the NIR pulses at the detector, yielding the time-domain THz waveform. The Fourier transform of this time-domain signal results in a frequency-domain transmission spectrum of the sample of interest.

The material used for this investigation was purchased from Sigma-Aldrich ( $\geq 98\%$  pure) and was used without further purification. The sample material, METH.HCl, was pulverized using a mortar and pestle to minimize particle size, limiting the possibility for radiation scattering. After being crushed to a fine powder, the sample material was homogeneously dispersed throughout a PTFE matrix by gentle stirring. The ratio of PTFE to sample was approximately 52:1. The mixture was then pressed into a pellet that was 1.6 mm thick and weighed 0.49 g. PTFE is used for the filler material because of its relative transparency in the THz region. Although THz absorptions are present in pure PTFE (particularly noticeable at low temperature),<sup>18,19</sup> these absorptions are negated by ratioing the Fourier transformed power spectrum of a pure PTFE blank against the Fourier transformed power spectrum of the sample pellet.

The THz radiation passing through the sample pellet is averaged a total of 32 times for each individual scan. The averaged waveform data is Fourier transformed to provide a frequency power spectrum, which is then ratioed against a frequency power spectrum created from a PTFE blank. The waveform data was uncorrected for any additional potential losses.<sup>20</sup> The ratioing of the power spectra yields a THz absorption spectrum in the frequency range of 10.0–100.0 cm<sup>-1</sup> with an instrument resolution of  $\sim 1.5$  cm<sup>-1</sup>. The final experimental THz spectra presented here are each an average of four of such acquisitions measured consecutively.

**B. Theoretical.** DFT calculations for both the solid-state METH.HCl and the isolated-molecule methamphetamine cation

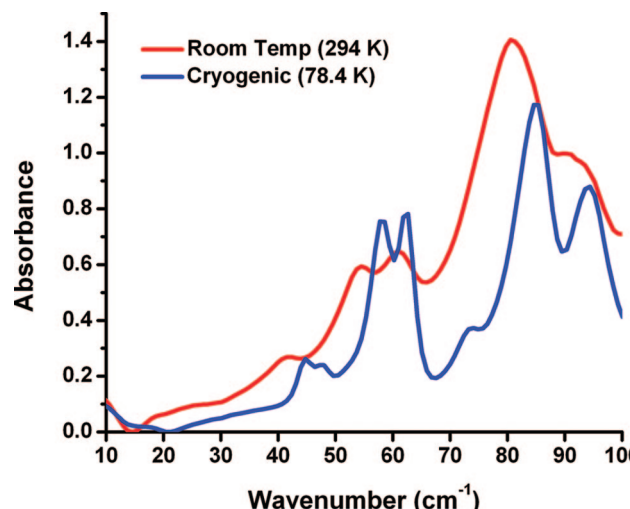


**Figure 1.** Experimental THz spectra of METH.HCl at room temperature, shown in red, and at 78.4 K, shown in blue.

(METH.H<sup>+</sup>) were performed using the DMol<sup>3</sup> (version 3.2)<sup>21,22</sup> software package. Isolated-molecule and solid-state calculations were completed with program option “fine” grid sizes (corresponding to a k-point separation of 0.04 Å<sup>-1</sup>), convergence criteria of  $\Delta E < 5 \times 10^{-7}$  hartree, and the DNP (double numerical with d and p polarization) basis set (comparable to a 6-31G(d,p) Gaussian-type basis set).<sup>21</sup> The eight generalized-gradient approximation (GGA) density functionals available in DMol<sup>3</sup> were used for this study, including the BLYP,<sup>23,24</sup> BOP,<sup>25</sup> PW91,<sup>26</sup> HCTH,<sup>27</sup> BP,<sup>23,28</sup> PBE,<sup>29,30</sup> RPBE,<sup>31</sup> and VWN-BP<sup>23,28,32</sup> functionals. Because the DNP basis set is used with all functionals, the presented calculations are referred to only by their functional in the text. Unlike other solid-state DFT packages, DMol<sup>3</sup> does not optimize lattice constants, meaning the molecules within the unit cell were optimized within the cell parameters specified by the recently published 90 K X-ray diffraction study of the title compound.<sup>33</sup> Crystal data for the compound are as follows: space group  $P_2_1$  ( $Z = 2$ ),  $a = 7.1022$  (11) Å,  $b = 7.2949$  (11) Å,  $c = 10.8121$  (17) Å,  $\alpha = 90.000^\circ$ ,  $\beta = 97.293^\circ$ ,  $\gamma = 90.000^\circ$ .

The infrared intensities provided for each of the solid-state modes are calculated via the difference dipole method. The IR intensities are calculated from the square of the change in dipole moments for the unit cell that result from atomic displacements along each normal-mode coordinate ( $d\mu/dq$ ) using a Mulliken population analysis, thereby considering only the IR intensity dependence on the change in dipole moment to estimate the actual intensity.<sup>34,35</sup>

### III. Results

**A. Experimental.** The room-temperature THz spectrum of METH.HCl from 10.0 to 100.0 cm<sup>-1</sup> is shown in Figure 1. Five absorption features are seen in this region. A weak absorption is visible at 42.3 cm<sup>-1</sup>, followed by two medium intensity features at 54.5 and 61.0 cm<sup>-1</sup>. A very strong and broad absorption occurs at 80.6 cm<sup>-1</sup>, whereas a final spectral feature, which could be considered to be a well-defined shoulder, is present at 90.0 cm<sup>-1</sup>. The room-temperature spectrum is in good agreement with earlier THz studies of the compound.<sup>12,13</sup> Experimental spectra presented in this study have been offset to place the minimum absorbance of the spectrum at zero.

The cryogenic (78.4 K) THz spectrum of METH.HCl is also displayed in Figure 1. As has been shown in other works,

**TABLE 1: Frequencies ( $\text{cm}^{-1}$ ) of THz Absorptions in METH.HCl Observed Experimentally at Liquid-Nitrogen and Room Temperatures<sup>a</sup>**

exptl (78.4 K)	exptl (294 K)	Li et al. <sup>12</sup>	Kanamori et al. <sup>13</sup>
44.8	42.3	41.0	41.5
<b>47.6</b>			
58.2	54.5	55.7	54.5
62.7	61.0	61.3	61
<b>74.5</b>			
85.0	80.6	81.0	82
94.4	90.0	90	

<sup>a</sup> Features listed in bold are previously unreported.

cryogenic cooling is an invaluable means for improving computational assignments by sharpening and uncovering the features contained in experimental THz spectra.<sup>36,37</sup> Peak shifting of 2–4  $\text{cm}^{-1}$  can be noted throughout the entire cryogenic spectrum. The shifts of the spectral features toward higher energy are likely caused by reductions in the lattice dimensions upon cooling.<sup>33</sup> The strongest absorption in the cryogenic spectrum is at 85.0  $\text{cm}^{-1}$ , with the next highest intensity features occurring at 62.7 and 58.2  $\text{cm}^{-1}$ , respectively. A fourth strong feature is present in the high-energy portion of the spectrum at 94.4  $\text{cm}^{-1}$ . The feature occurring at 94.4  $\text{cm}^{-1}$  attains a higher absorbance value than the peaks at 62.7 and 58.2  $\text{cm}^{-1}$ ; however, part of the perceived intensity of this feature can likely be attributed to a slightly rising baseline; therefore, it is deemed slightly less intense. Three lower intensity features include a weak single peak at 74.5  $\text{cm}^{-1}$ , which is not visible in the room-temperature spectrum, and a second pair with its two peaks centered at 44.8 and 47.6  $\text{cm}^{-1}$ , respectively. Within the latter pair, the lower energy peak exhibits slightly higher intensity. These two features are only resolved in the cryogenic spectrum, appearing as a single feature in the room-temperature study. Table 1 provides a list of the cryogenic and room-temperature absorptions determined in the current study and in two prior room-temperature studies.<sup>12,13</sup>

**B. Theoretical. 1. Comparison of Experimental and Simulated Molecular Structures.** Single-crystal X-ray diffraction and calculated solid-state DFT structural data for METH.HCl are provided in Table 2 (bond lengths) and Table 3 (bond angles). For reference, Figure 2 provides the labeling scheme of the (+)-methamphetamine molecule. Deviations in the calculated bond lengths from experiment<sup>33</sup> are graphically depicted in Figure 3 for ease of comparison of both the solid-state and the isolated molecule. The Figure shows the trend of improved agreement with the experimental values in the solid-state-calculated geometries relative to the isolated-molecule geometries. Figure 3 also shows the general overestimation of the bond lengths for both the solid-state and the isolated molecule in comparison with experiment. The bond length agreement for the optimized solid-state geometries with the experimental value is best for the HCTH functional, as has been observed in previous work,<sup>34,35</sup> followed by the PW91 and VWN-BP functionals, respectively, on the basis of root-mean-square deviation (RMSD) comparisons. The bond angle agreement for the solid-state geometry provided by the BP functional is best, closely followed by the VWN-BP and PW91 functionals, again on the basis of RMSD comparisons.

Structural data for the protonated methamphetamine (METH.H<sup>+</sup>) isolated molecule is provided in Tables 4 (bond lengths) and 5 (bond angles). The METH.H<sup>+</sup> is the comparison-appropriate representation of the three possible isolated-molecule configurations (the protonated and two neutral configurations),

a point that received previous attention for the reassignment of the THz spectrum of MDMA.HCl.<sup>38</sup> Only data for the protonated form is provided here because the local geometry of the nitrogen and protons of the H<sup>+</sup>...Cl<sup>-</sup> network clearly indicated that the proton is at the nitrogen lone pair.<sup>38</sup> The bond lengths of the METH.H<sup>+</sup> isolated molecule calculated using the HCTH functional provided the best agreement with experiment, as they did with the solid-state calculated bond lengths. The PW91 and PBE functionals provided the second and third best fits, respectively. In terms of bond angles, the RMSD values were best for the BLYP functional, followed by the PBE and BOP functionals.

The molecular geometries determined by the solid-state optimizations are categorically better than those determined for the isolated molecule when compared by RMSDs. All but three of the solid-state optimizations (BLYP, BOP, RPBE) provided improved RMSD values for the bond lengths over the best value determined from the isolated-molecule calculations. In bond angle RMSD comparisons, the worst solid-state bond angle RMSD was still substantially better than the best value determined from the isolated-molecule geometry optimizations. The largest difference in bond length RMSD between the solid-state and isolated molecule is the N<sub>1</sub>–C<sub>3</sub> bond (average overestimation = 0.0430 Å for isolated molecule, 0.0046 Å for solid state), and in a lesser sense, the C<sub>1</sub>–N<sub>1</sub> bond (average overestimation = 0.0224 Å for isolated molecule, 0.0059 Å for solid state). The lengths of these two bonds are rather poorly estimated by the isolated-molecule calculations because of the absence of hydrogen bonding in the single-molecule calculation. The large difference in the lengths predicted by the isolated-molecule and the solid-state calculations for the length of the bond between the nitrogen and the hydrogen nearest to the chloride position is also of interest. This average distance in the solid-state calculations is 1.0548 Å, whereas the isolated-molecule calculations predict a length of 1.0283 Å. The hydrogen position is not determined accurately enough by X-ray diffraction to determine which simulation is more accurate; however, the difference between the two predictions is clearly connected to hydrogen bonding.

**2. Comparison of Experimental and Simulated Terahertz Spectra.** The solid-state vibrational predictions, using the 90 K crystal cell parameters for all eight functionals, are plotted along with the cryogenic experimental THz spectrum in Figure 4. This Figure is provided to show the quality of the fit achieved with the DNP basis set and each of the eight GGA density functionals. The theoretical predictions are plotted as both stick plots and convolved plots with an empirical Lorentzian line shape (2.25  $\text{cm}^{-1}$  full width at half-maximum) to reproduce the observed cryogenic spectrum more realistically. The quality of fit varies substantially across the eight functionals in both relative intensities and peak positions. Whereas the BOP functional can be argued as providing the best fit to the experimental spectrum by visual inspection (specifically in the improved agreement in spectral intensity over the BP functional for the two features centered at 60  $\text{cm}^{-1}$ ), statistical analysis of the simulations shows that the BP functional actually provides the most accurate overall simulation of the experimental data. The solid-state BP calculation predicts a total of 13 vibrational modes in the range of the experimental spectrum. All 13 of the modes are IR-active and are responsible for the seven observed spectral features.

The simulation based on the BP functional is determined to reproduce the experimental spectra most accurately by the calculation of RMSD values for deviations in both spectral intensity and vibrational frequency from the experimental

**TABLE 2:** [Functional]/DNP Solid-State Bond Lengths (Angstroms) and Bond RMSDs for METH.HCl<sup>a</sup>

bond	exptl	BLYP	BOP	BP	HCTH	PBE	PW91	RPBE	VWN-BP
C <sub>1</sub> —N <sub>1</sub>	1.4848	1.5012	1.5019	1.4883	1.4780	1.4868	1.4868	1.4944	1.4881
N <sub>1</sub> —C <sub>3</sub>	1.5097	1.5260	1.5276	1.5111	1.5011	1.5093	1.5092	1.5192	1.5108
C <sub>2</sub> —C <sub>3</sub>	1.5178	1.5269	1.5288	1.5193	1.5181	1.5186	1.5178	1.5262	1.5189
C <sub>3</sub> —C <sub>4</sub>	1.5355	1.5494	1.5518	1.5407	1.5373	1.5401	1.5393	1.5484	1.5404
C <sub>4</sub> —C <sub>5</sub>	1.5157	1.5161	1.5174	1.5093	1.5028	1.5089	1.5081	1.5153	1.5090
C <sub>5</sub> —C <sub>6</sub>	1.3944	1.4046	1.4057	1.4023	1.3970	1.4023	1.4013	1.4064	1.4021
C <sub>6</sub> —C <sub>7</sub>	1.3853	1.3988	1.3996	1.3964	1.3911	1.3967	1.3954	1.4004	1.3962
C <sub>7</sub> —C <sub>8</sub>	1.3903	1.3999	1.4010	1.3978	1.3927	1.3981	1.3970	1.4016	1.3976
C <sub>8</sub> —C <sub>9</sub>	1.3828	1.4006	1.4015	1.3982	1.3936	1.3981	1.3972	1.4021	1.3979
C <sub>9</sub> —C <sub>10</sub>	1.3937	1.3991	1.4005	1.3970	1.3916	1.3975	1.3960	1.4018	1.3968
C <sub>10</sub> —C <sub>5</sub>	1.3883	1.4063	1.4077	1.4040	1.4000	1.4042	1.4030	1.4082	1.4037
RMSD	0.0130	0.0142	0.0086	0.0073	0.0087	0.0080	0.0126	0.0085	

<sup>a</sup> Atom labels provided in Figure 2. Experimental values (exptl) are taken from ref 33.

**TABLE 3:** [Functional]/DNP Solid-State Bond Angles (Degrees) and Angle RMSDs for METH.HCl<sup>a</sup>

angle	exptl	BLYP	BOP	BP	HCTH	PBE	PW91	RPBE	VWN-BP
C <sub>1</sub> —N <sub>1</sub> —C <sub>3</sub>	116.324	116.867	117.094	116.304	117.461	116.490	116.318	116.972	116.294
N <sub>1</sub> —C <sub>3</sub> —C <sub>2</sub>	109.893	110.449	110.468	110.457	110.949	110.487	110.476	110.569	110.462
N <sub>1</sub> —C <sub>3</sub> —C <sub>4</sub>	106.142	106.409	106.439	106.505	106.771	106.489	106.494	106.546	106.503
C <sub>2</sub> —C <sub>3</sub> —C <sub>4</sub>	113.863	114.157	114.292	113.948	113.816	113.997	113.955	114.196	113.951
C <sub>3</sub> —C <sub>4</sub> —C <sub>5</sub>	113.370	113.681	113.537	113.591	113.362	113.606	113.644	113.227	113.591
C <sub>4</sub> —C <sub>5</sub> —C <sub>6</sub>	120.798	120.605	120.591	120.780	120.772	120.738	120.755	120.684	120.780
C <sub>4</sub> —C <sub>5</sub> —C <sub>10</sub>	120.540	120.760	120.814	120.676	120.778	120.688	120.679	120.796	120.675
C <sub>5</sub> —C <sub>6</sub> —C <sub>7</sub>	120.517	120.630	120.643	120.596	120.753	120.621	120.591	120.720	120.595
C <sub>6</sub> —C <sub>7</sub> —C <sub>8</sub>	120.512	120.337	120.382	120.470	120.439	120.405	120.443	120.390	120.471
C <sub>7</sub> —C <sub>8</sub> —C <sub>9</sub>	119.340	119.499	119.457	119.397	119.278	119.455	119.436	119.374	119.400
C <sub>8</sub> —C <sub>9</sub> —C <sub>10</sub>	120.136	120.087	120.099	120.050	120.234	120.051	120.032	120.180	120.048
C <sub>9</sub> —C <sub>10</sub> —C <sub>5</sub>	120.820	120.808	120.819	120.939	120.840	120.892	120.929	120.812	120.939
C <sub>10</sub> —C <sub>5</sub> —C <sub>6</sub>	118.660	118.628	118.588	118.538	118.448	118.570	118.559	118.518	118.539
RMSD	0.280	0.328	0.210	0.479	0.225	0.219	0.320	0.211	

<sup>a</sup> Atom labels provided in Figure 2. Experimental values (exptl) are taken from ref 33.

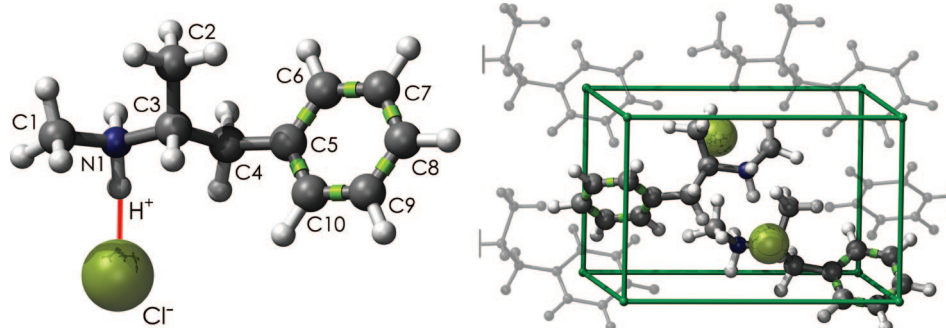


**Figure 2.** (+)-Methamphetamine molecule shown with the nearest crystal chlorine position (left) and the crystal unit cell of (+)-METH.HCl. Figure rendered with NanoEngineer-1<sup>39</sup> and POV-Ray.<sup>40</sup>

spectra. The difference in spectral intensity is determined by calculating the residual difference in intensity between the experimental spectra and the best-fit scaled intensity simulation for each of the eight density functionals. The calculated RMSD values for the spectral intensity are provided in Table 6. On the basis of the reproduction of total spectral intensity, the BP functional most accurately replicates the experimental spectra, attaining the lowest residual intensity RMSD value, followed by the PBE and BOP density functionals, respectively, with the second and third lowest values.

Because the BP functional was the most effective in simulating the experimental spectral intensity, it was used as the starting point in evaluating the predictive power of each of the eight functionals for accurately modeling the experimentally observed frequencies. The determination of a best-fit simulation by frequency RMSD was done by first assigning five specific vibrational modes calculated at the BP level to experimental

features at 44.8, 58.2, 74.5, 85.0, and 94.4 cm<sup>-1</sup>. The corresponding motions of each of the five calculated BP modes at these assignments were then located in the simulations from the remaining functionals. This method provides a quantitative gauge of the ability of each functional to reproduce the experimentally observed frequencies. The results are listed in Table 6. On the basis of RMSD values for the frequency deviations, the VWN-BP functional was determined to provide the most accurate vibrational frequencies, with the related BP functional providing a very close second-best RMSD value. The PBE and PW91 functionals followed with the third-best RMSD values. With the BP functional providing the best simulation of the experimental spectral intensity and the nearly best reproduction of the experimental spectral frequencies, it has been determined that the BP functional is the best overall performer in the simulation of the METH.HCl spectrum.

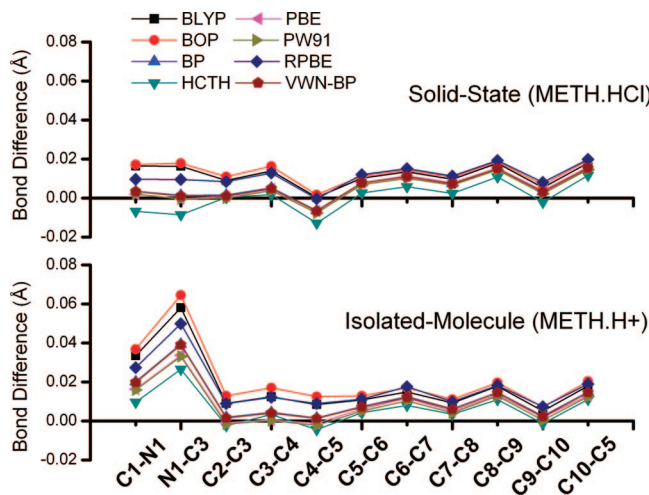


**Figure 3.** Deviations in calculated bond lengths from experiment for the solid-state (METH.HCl, top) and for the isolated-molecule (METH.H<sup>+</sup>, bottom) DMol<sup>3</sup> minimum-energy geometries.

The PBE functional is determined to provide the second-best overall fit to the experimental data. The PBE simulation provides the second-best fit in terms of spectral intensity and is tied for third for best fit in terms of frequency to the experimental data. The VWN-BP functional provides the best fit to the experiment in terms of frequency, albeit by a very small margin over the BP functional, and the fifth-best experimental reproduction in terms of spectral intensity. Therefore, the VWN-BP functional is considered to provide the third-best simulation. The summary of the statistical analyses of the PBE, VWN-BP, and BP

calculations is that multiple functionals are capable of providing reasonable simulations of experimental THz spectra.

The significant differences in the simulations are partially explained by the different numbers of modes predicted to occur in the experimental range across the functionals, ranging from nine for the HCTH functional to 14 for the BOP functional. All of the predicted modes in the experimental range, regardless of functional, are IR-active. The vibrational frequencies predicted for each of the eight functionals by both the solid-state and isolated-molecule methods are provided in Table 7. The differences in the calculated frequencies and the number of modes in a given range are reasonably expected to vary across a series of functionals because of inherent differences in the formulation of each density functional. The differences in the formulation can lead to substantial shifting in the predicted location of a given mode, potentially leading to a mode being found in the experimental range by several functionals, but predicted to occur outside of the experimental range by another.

### 3. Terahertz Mode Assignments Based on the BP/DNP Simulated Spectrum.

On the basis of the density functional comparisons, the BP simulated solid-state spectrum provides the best agreement with the experimental cryogenic spectrum, offering the best result in terms of both peak positions and relative intensities of the IR-active modes. It is therefore used to assign the experimental absorption features to specific atomic motions. The assignment of the features within the experimental THz spectrum is accomplished using the results provided by both the solid-state and isolated-molecule BP simulated spectra. (Isolated-molecule calculations serve as the basis for assigning internal modes in the solid-state calculations.)

**TABLE 4: [Functional]/DNP Isolated-Molecule Bond Lengths (Angstroms) and Bond RMSDs for METH.H<sup>+</sup><sup>a</sup>**

bond	exptl	BLYP	BOP	BP	HCTH	PBE	PW91	RPBE	VWN-BP
C <sub>1</sub> -N <sub>1</sub>	1.4848	1.5182	1.5216	1.5049	1.4944	1.5011	1.5008	1.5122	1.5046
N <sub>1</sub> -C <sub>3</sub>	1.5097	1.5678	1.5742	1.5491	1.5362	1.5434	1.5428	1.5596	1.5487
C <sub>2</sub> -C <sub>3</sub>	1.5178	1.5268	1.5306	1.5197	1.5154	1.5170	1.5162	1.5267	1.5194
C <sub>3</sub> -C <sub>4</sub>	1.5355	1.5479	1.5525	1.5399	1.5388	1.5360	1.5357	1.5477	1.5395
C <sub>4</sub> -C <sub>5</sub>	1.5157	1.5241	1.5282	1.5172	1.5113	1.5145	1.5134	1.5246	1.5170
C <sub>5</sub> -C <sub>6</sub>	1.3944	1.4052	1.4073	1.4018	1.3987	1.4005	1.3995	1.4056	1.4015
C <sub>6</sub> -C <sub>7</sub>	1.3853	1.4002	1.4023	1.3978	1.3933	1.3971	1.3957	1.4029	1.3975
C <sub>7</sub> -C <sub>8</sub>	1.3903	1.3996	1.4014	1.3965	1.3937	1.3953	1.3945	1.4002	1.3962
C <sub>8</sub> -C <sub>9</sub>	1.3828	1.4007	1.4025	1.3975	1.3937	1.3963	1.3956	1.4010	1.3973
C <sub>9</sub> -C <sub>10</sub>	1.3937	1.3988	1.4009	1.3962	1.3924	1.3956	1.3941	1.4011	1.3959
C <sub>10</sub> -C <sub>5</sub>	1.3883	1.4063	1.4087	1.4032	1.3994	1.4014	1.4008	1.4072	1.4030
RMSD	0.0231	0.0262	0.0156	0.0103	0.0134	0.0129	0.0209	0.0154	

<sup>a</sup> Atom labels provided in Figure 2. Experimental values (exptl) are taken from ref 33.

**TABLE 5: [Functional]/DNP Isolated-Molecule Bond Angles (Degrees) and Angle RMSDs for METH.H<sup>+</sup><sup>a</sup>**

angle	exptl	BLYP	BOP	BP	HCTH	PBE	PW91	RPBE	VWN-BP
C <sub>1</sub> -N <sub>1</sub> -C <sub>3</sub>	116.324	116.972	117.328	116.919	117.586	116.719	116.661	117.578	116.919
N <sub>1</sub> -C <sub>3</sub> -C <sub>2</sub>	109.893	109.651	109.710	109.830	110.317	109.912	109.810	109.926	109.826
N <sub>1</sub> -C <sub>3</sub> -C <sub>4</sub>	106.142	107.237	107.250	107.438	107.490	107.373	107.443	107.201	107.440
C <sub>2</sub> -C <sub>3</sub> -C <sub>4</sub>	113.863	114.820	114.998	114.522	114.769	114.276	114.351	114.820	114.520
C <sub>3</sub> -C <sub>4</sub> -C <sub>5</sub>	113.370	112.569	112.703	112.153	112.814	112.228	111.931	112.497	112.154
C <sub>4</sub> -C <sub>5</sub> -C <sub>6</sub>	120.798	120.785	120.785	120.823	121.190	120.864	120.856	120.904	120.824
C <sub>4</sub> -C <sub>5</sub> -C <sub>10</sub>	120.540	120.180	120.240	120.115	120.007	120.025	120.025	120.048	120.114
C <sub>5</sub> -C <sub>6</sub> -C <sub>7</sub>	120.517	120.476	120.499	120.458	120.572	120.468	120.421	120.516	120.457
C <sub>6</sub> -C <sub>7</sub> -C <sub>8</sub>	120.512	120.087	120.101	120.080	120.210	120.032	120.082	120.021	120.084
C <sub>7</sub> -C <sub>8</sub> -C <sub>9</sub>	119.340	119.824	119.813	119.842	119.601	119.862	119.855	119.846	119.842
C <sub>8</sub> -C <sub>9</sub> -C <sub>10</sub>	120.136	120.085	120.089	120.074	120.164	120.091	120.055	120.139	120.070
C <sub>9</sub> -C <sub>10</sub> -C <sub>5</sub>	120.820	120.492	120.521	120.483	120.643	120.436	120.468	120.429	120.485
C <sub>10</sub> -C <sub>5</sub> -C <sub>6</sub>	118.660	119.035	118.974	119.062	118.803	119.111	119.118	119.048	119.062
RMSD	0.557	0.600	0.611	0.643	0.573	0.632	0.646	0.611	

<sup>a</sup> Atom labels provided in Figure 2. Experimental values (exptl) are taken from ref 33.

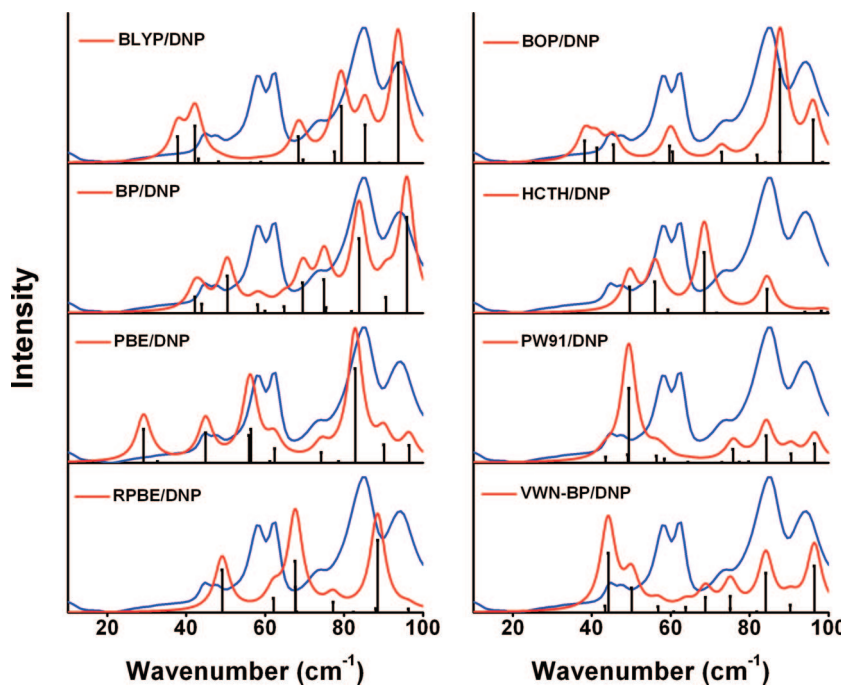


**Figure 4.** Comparison of the simulated and experimental (78.4 K) solid-state THz spectrum of METH.HCl from 10 to 100  $\text{cm}^{-1}$ . The experimental spectrum is shown in blue. Black lines represent the calculated infrared intensity of each predicted mode. The red trace is a convolved plot of the theoretical vibrational modes using a  $2.25 \text{ cm}^{-1}$  (fwhm) Lorentzian line shape.

**TABLE 6: Statistical Analyses of the Quality of Fit of the Solid-State DFT Simulations to the Cryogenic Experimental Spectrum of METH.HCl**

RMSD of residual intensity								
BLYP	BOP	BP	HCTH	PBE	PW91	RPBE	VWN-BP	
0.305	0.293	0.233	0.465	0.256	0.464	0.414	0.335	
RMSD of calculated frequency for five correlated vibrational modes								
BLYP	BOP	BP	HCTH	PBE	PW91	RPBE	VWN-BP	exptl feature
58.9	45.5	42.2	49.6	44.9	43.5	49.2	43.4	44.8
48.2	55.7	58.1	68.5	56.4	56.4	62.1	56.8	58.2
77.6	84.0	74.9	84.4	74.2	73.1	88.0	75.1	74.5
85.3	87.7	83.9	94.1	82.8	84.2	96.3	84.1	85.0
93.7	96.1	95.9	110.8	96.5	96.6	113.9	96.4	94.4
7.8	4.6	1.4	10.8	1.6	1.6	12.0	1.3	

A crystal unit cell containing  $M$  molecules with  $N$  atoms contains  $3N-6M$  internal modes (those modes associated with intramolecular motions),  $6M-3$  external modes (those modes associated with relative motions between the  $M$  molecules, such as rotations and translations), and three acoustic modes. The crystal cell of METH.HCl contains two molecules ( $Z = 2$ ), with each asymmetric unit containing 28 atoms. METH.HCl contains nine external vibrational modes. These nine modes consist of three optical translational modes and six optical rotational modes.

The assignment and description of the labeled modes are provided in Table 8. The solid-state vibrations present in METH.HCl can generally be assigned as either internal (molecular bending and torsions) or external modes. It is observed that some of the modes are mixed, exhibiting both internal and external character, which adds complexity to their assignment. The classification of the 13 BP-predicted modes present in the experimental frequency range has been made based on the largest contributor to the character of the mode. The vibrational modes present in the cryogenic solid-state THz spectrum of METH.HCl are labeled in Figure 5 as modes a–m. The calculated intensity of the least intense mode (j) is roughly 1.5%

of the calculated intensity of the most intense mode (m). To highlight further the inability of the isolated-molecule calculations to simulate solid-state THz spectra accurately, a plot of the three vibrational modes predicted by the isolated-molecule BP calculation against the cryogenic spectrum is provided in Figure 6.

#### IV. Discussion

Measuring the THz spectrum of METH.HCl at liquid-nitrogen temperatures provides a spectrum with significantly improved spectral resolution over room-temperature studies, which, in turn, provides a more complete characterization of the compound. In the case of METH.HCl, the improvements not only provided a more defined spectrum but also revealed additional features that were not observed at room temperature. These are important for not only the proper characterization of the compound experimentally but also the development and improvement of methods to simulate, predict, and assign experimental THz spectra.

Assignment of the experimental spectrum is found to be possible only by use of solid-state DFT. The BP calculation of

**TABLE 7: List of the 13 Lowest-Frequency Normal Modes of Solid-State METH.HCl and the Four Lowest-Frequency Normal Modes of METH.H<sup>+</sup> [Functional/DNP]<sup>a</sup>**

mode	BLYP	BOP	BP	HCTH	PBE	PW91	RPBE	VWN-BP
a	<b>37.8</b>	<b>25.2</b>	<b>42.2</b>	<b>49.6</b>	<b>29.2</b>	<b>43.5</b>	<b>49.1</b>	<b>43.4</b>
b	<b>42.2</b>	<b>38.2</b>	<b>43.9</b>	<b>56.0</b>	<b>32.7</b>	<b>49.1</b>	<b>62.1</b>	<b>44.2</b>
c	<b>43.1</b>	<b>41.3</b>	<b>50.4</b>	<b>59.3</b>	<b>44.9</b>	<b>49.4</b>	<b>67.6</b>	<b>50.1</b>
d	<b>48.2</b>	<b>45.5</b>	<b>58.1</b>	<b>68.5</b>	<b>55.9</b>	<b>56.4</b>	<b>67.7</b>	<b>56.8</b>
e	<b>56.3</b>	<b>55.7</b>	<b>60.0</b>	<b>71.7</b>	<b>56.4</b>	<b>58.4</b>	<b>68.0</b>	<b>60.8</b>
f	<b>58.9</b>	<b>59.7</b>	<b>64.8</b>	<b>84.4</b>	<b>61.2</b>	<b>64.4</b>	<b>77.2</b>	<b>63.8</b>
g	<b>68.4</b>	<b>60.5</b>	<b>69.5</b>	<b>94.0</b>	<b>62.4</b>	<b>73.0</b>	<b>82.4</b>	<b>68.8</b>
h	<b>69.6</b>	<b>72.9</b>	<b>74.9</b>	<b>98.2</b>	<b>74.2</b>	<b>75.8</b>	<b>88.0</b>	<b>75.1</b>
i	<b>77.6</b>	<b>81.9</b>	<b>75.4</b>	<b>99.8</b>	<b>78.6</b>	<b>77.4</b>	<b>88.5</b>	<b>75.1</b>
j	<b>79.3</b>	<b>84.0</b>	<b>81.9</b>	110.8	<b>82.8</b>	<b>79.8</b>	<b>96.3</b>	<b>81.8</b>
k	<b>85.3</b>	<b>87.7</b>	<b>83.8</b>	114.3	<b>90.1</b>	<b>84.2</b>	107.9	<b>84.1</b>
l	<b>88.9</b>	<b>87.7</b>	<b>90.6</b>	125.8	<b>96.5</b>	<b>90.5</b>	113.3	<b>90.3</b>
m	<b>93.7</b>	<b>96.1</b>	<b>95.9</b>	138.9	101.7	<b>96.5</b>	132.1	<b>96.4</b>
mode	BLYP	BOP	BP	HCTH	PBE	PW91	RPBE	VWN-BP
1	<b>43.0 (0.75)</b>	<b>42.3 (1.28)</b>	<b>41.7 (0.39)</b>	<b>88.4 (1.87)</b>	<b>65.4 (1.12)</b>	<b>39.8 (0.25)</b>	<b>62.7 (0.62)</b>	<b>42.4 (0.40)</b>
2	<b>56.5 (0.35)</b>	<b>52.5 (0.09)</b>	<b>58.4 (0.65)</b>	112.5 (0.72)	<b>72.3 (0.15)</b>	<b>57.4 (0.81)</b>	<b>79.8 (0.26)</b>	<b>58.2 (0.64)</b>
3	<b>85.2 (1.11)</b>	<b>83.1 (0.84)</b>	<b>93.7 (1.12)</b>	140.3 (0.19)	106.4 (1.21)	<b>90.5 (1.16)</b>	<b>106.6 (0.70)</b>	<b>93.9 (1.12)</b>
4	108.0 (3.17)	89.3 (2.52)	101.6 (3.27)	169.9 (3.07)	115.3 (3.47)	95.8 (3.35)	157.5 (4.24)	101.7 (3.29)

<sup>a</sup> Calculated IR intensity (km/mol) is included in parentheses for the isolated-molecule normal modes. Modes within the experimental region (below  $\sim 100$  cm<sup>-1</sup>) are bolded.

**TABLE 8: Vibrational Mode Assignments of METH.HCl at the BP/DNP Level of Theory**

mode	solid state	description <sup>a,b</sup>	% of total intensity	associated isolated-molecule or external mode
a	42.2	optical translation along crystal C axis, methyl rotors (IP)	4.8	OT (C axis)
b	43.9	methyl rotors (OOP), optical rotation (OOP) along crystal C axis	2.7	OR (C axis)
c	50.4	N <sub>1</sub> —C <sub>3</sub> (OOP) torsion, optical rotation (OOP) along crystal B axis	11.1	OR (B axis) + 101.6 cm <sup>-1</sup>
d	58.1	optical rotation (OOP) along crystal B axis, chloride (OOP) translation along crystal A axis	2.5	OR (B axis) + OT Cl (A axis)
e	60.0	optical translation along crystal B axis	0.5	OT (B axis)
f	64.8	optical rotation (IP) along crystal C axis, N <sub>1</sub> —C <sub>3</sub> torsion (IP)	1.9	OR (C axis) + 101.6
g	69.5	optical rotation (OOP) along crystal C axis, N <sub>1</sub> —C <sub>3</sub> torsion (OOP)	9.1	OR (C axis) + 101.6
h	74.9	phenyl rotors (OOP), chloride translation (OOP) along crystal C axis	10.0	OT Cl (C axis) + 41.7
i	75.4	optical rotation (IP) along crystal A axis	1.6	OR (A axis)
j	81.9	phenyl rotors (OOP)	0.4	41.7
k	83.9	N <sub>1</sub> —C <sub>3</sub> torsion (IP), chloride (OOP) translation along crystal C axis	22.2	OT Cl (C axis) + 101.6
l	90.6	C <sub>3</sub> —C <sub>4</sub> torsion (OOP)	4.7	58.4
m	95.9	C <sub>3</sub> —C <sub>4</sub> torsion (OOP), chloride translation (IP) along crystal A axis	28.5	OT Cl (A axis) + 58.4
mode	isolated	description		
1	41.7	phenyl rotor		
2	58.4	C <sub>3</sub> —C <sub>4</sub> torsion		
3	93.7	C <sub>3</sub> —C <sub>4</sub> —C <sub>5</sub> butterfly motion		
4	101.6	N <sub>1</sub> —C <sub>3</sub> torsion		

<sup>a</sup> OR: optical rotation, OT: optical translation. <sup>b</sup> IP: in-phase, OOP: out-of-phase for the relative intramolecular motions of the molecules in the Z = 2 unit cell.

the isolated molecule predicts only three vibrational modes in an experimental range (with a fourth mode just outside the range) composed of at least seven experimental features. By incorporating the interactions present in the crystal cell, the solid-state calculation is able to reproduce the experimental absorption positions and intensities accurately, whereas the isolated-molecule calculations clearly fail.

The BP functional simulation provides the best overall fit of the experimental data. Minor deviations from the experimental spectra can be seen, such as the shift to slightly lower energy for modes a and b and to slightly higher energy for mode c. The most substantial deviations in the theoretical simulation are due to the calculated intensities of modes d, e, and f. The intensities calculated for these modes are significantly lower than the intensity observed in the experimental spectrum. However, the frequencies determined for these modes appear to align quite well with experiment. As predicted, the d and f

modes are assigned to the two major peaks, leaving the e mode to account for additional structure on the d peak. The calculated intensity for mode h appears to be slightly overestimated, as does the intensity for mode g. The frequency predicted for mode g is also questionable because it is a moderately intense mode but is located roughly between two experimental features. This makes the assignment of this mode to a particular experimental feature difficult. The predicted intensity for modes k and m is the inverse of what is seen in the experimental spectrum. This deviation is not necessarily wrong because the experimental feature related to the calculated mode m occurs quite near to the upper limit of instrument bandwidth, which could lead to a less accurate experimental intensity. Additionally, some of the deviation in intensity from the experimental data may be due to the presence of a slightly rising baseline in the experimental spectrum. The quality of fit provided by the BP functional is of interest because this functional was not the best performer in

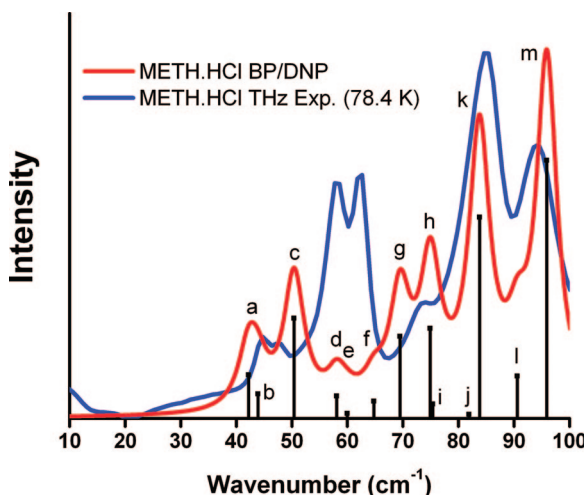


**Figure 5.** Comparison of the BP/DNP and cryogenic solid-state THz spectra for METH.HCl. The experiment is shown in blue. The infrared intensity of the modes predicted using the BP density functional are shown as black lines. The red trace is a convolved plot of the predicted modes using a  $2.25\text{ cm}^{-1}$  Lorentzian line shape. Mode labels are detailed in Table 7.

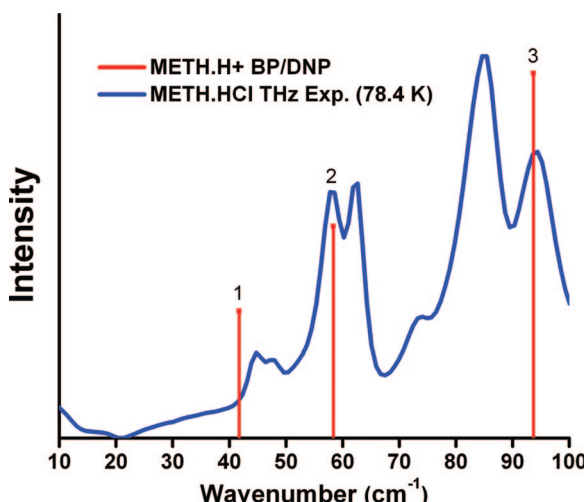


**Figure 6.** Comparison of the experimental solid-state THz spectrum of METH.HCl to the vibrational modes predicted by the BP isolated-molecule calculation. The experimental spectrum is shown in blue. The infrared intensity of the predicted modes is shown as red lines.

reproducing the solid-state bond lengths of METH.HCl and was actually the third-best performer in terms of the replication of the bond lengths when judged by RMSD.

The structural data highlight an interesting paradox because the HCTH functional most accurately reproduces the experimental geometry when judged by RMSD but provides a very poor fit to the experimental THz spectrum in terms of both peak position and intensity when compared with the other GGA functionals employed in this study. This is particularly apparent when judged against the simulation provided by the BP functional, which provides a good reproduction of the experimental THz data. The BP functional provides the best agreement with the experimental bond angles of any of the eight functionals when compared on the basis of RMSD. The possible connection between the ability of a functional to model the bond angles accurately and its ability to calculate experimental vibrational frequencies accurately is indicated by the same four functionals providing the best RMSD values in these two categories. The four functionals are ranked in the same order of quality, except

for the BP and VWN-BP functionals, which alternate in providing the best RMSD value for bond angle and frequency.

Differences in density functional formulation will of course lead to differences in the quality of the output and the resulting simulations, in terms of both structural agreement and spectral agreement. This would infer that as additional spectral simulations are performed and a much larger data set of analyses is available from additional studies within the THz and related communities, only certain functionals will be deemed “useful” for THz modeling, and others will be deemed ineffective. The new set of experimental data generated from the combination of solid-state DFT and terahertz (and other low-energy) spectroscopy may also serve the purpose of providing additional criteria for testing the accuracy of new density functionals. One goal of the work reported here is to highlight the substantial differences between density functionals in their abilities to simulate THz spectra properly. Disagreement between the vibrational analyses and the structural analyses using solid-state DFT methods is not without precedent, having been the focus of previous density functional survey papers that employ the same levels of theory for structural comparisons and THz simulations.<sup>34,35</sup> It is clear that proper assignment will only become more difficult as the sizes of the systems and the number of vibrational modes within the THz region for a sample increase, making the need for accurate solid-state treatments all the greater.

## V. Conclusions

The THz vibrational spectrum of METH.HCl at room temperature and liquid-nitrogen temperature has been measured from  $10.0$  to  $100.0\text{ cm}^{-1}$  and has been assigned using solid-state DFT calculations. The cryogenic study reveals multiple low-intensity features not previously reported. The solid-state calculations, through the inclusion of the crystal interactions, are able to reproduce the structural parameters of the crystalline compound accurately and provide excellent agreement with the experimental THz spectrum. The assignment of the spectrum has been accomplished on the basis of the vibrational frequencies and IR intensities determined by solid-state normal-mode analyses using the BP functional in combination with the DNP basis set. The analysis indicates that the seven features visible in the experimental spectrum are composed of a total of 13 IR-active vibrational modes, with approximately 90% of the observed spectral intensity coming from external vibrational modes. Isolated-molecule calculations are unable to provide an accurate reproduction of the spectral features because only three modes are predicted in the experimental range. This study is an example of the capabilities of solid-state DFT and highlights the necessity of considering the crystal cell to simulate and interpret the THz spectra of molecular solids properly.

**Acknowledgment.** P.M.H. thanks the Syracuse University STEM and GEM Fellowship programs for their continued support. We also acknowledge Dr. John M. Belote (Syracuse University) for his assistance in procuring the research samples.

## References and Notes

- (1) Hu, Y.; Huang, P.; Guo, L.; Wang, X.; Zhang, C. *Phys. Lett. A* **2006**, *359*, 728.
- (2) Leahy-Hoppa, M. R.; Fitch, M. J.; Zheng, X.; Hayden, L. M.; Osiander, R. *Chem. Phys. Lett.* **2007**, *434*, 227.
- (3) Federici, J. F.; Schuklin, B.; Huang, F.; Gary, D.; Barat, R.; Oliveira, F.; Zimdars, D. *Semicond. Sci. Technol.* **2005**, *20*, S266.
- (4) Taday, P. F. *Philos. Trans. R. Soc. London, Ser. A* **2004**, *362*, 351.
- (5) Zeitler, J. A.; Taday, P. F.; Newham, D. A.; Pepper, M.; Gordon, K. C.; Rades, T. *J. Pharm. Pharmacol.* **2007**, *59*, 209.

- (6) Wang, G.; Shen, J.; Jia, Y. *J. Appl. Phys.* **2007**, *102*, 013106/1.  
(7) Dobroiu, A.; Sasaki, Y.; Shibuya, T.; Otani, C.; Kawase, K. *Proc. IEEE* **2007**, *95*, 1566.  
(8) Lu, M.; Shen, J.; Li, N.; Zhang, Y.; Zhang, C.; Liang, L.; Xu, X. *J. Appl. Phys.* **2006**, *100*, 103104/1.  
(9) Levine, B. *Principles of Forensic Toxicology*, 2nd ed.; 2003.  
(10) Cho, A. K. *Science* **1990**, *249*, 631.  
(11) Allen, A.; Cantrell, T. S. *Forensic Sci. Int.* **1989**, *42*, 183.  
(12) Li, N.; Shen, J.; Sun, J.; Liang, L.; Xu, X.; Lu, M.; Yan, J. *Opt. Express* **2005**, *13*, 6750.  
(13) Kanamori, T.; Tsujikawa, K.; Iwata, Y. T.; Inoue, H.; Ohtsuru, O.; Kishi, T.; Hoshina, H.; Otani, C.; Kawase, K. In *IRMMW-THz 2005, Joint 30th International Conference on Infrared and Millimeter Waves and 13th International Conference on Terahertz Electronics*, Williamsburg, VA, Sept. 19–23, 2005; Vol. 1, p 180.  
(14) Kawase, K.; Ogawa, Y.; Watanabe, Y. *Opt. Express* **2003**, *11*, 2549.  
(15) Nahata, A.; Weling, A. S.; Heinz, T. F. *Appl. Phys. Lett.* **1996**, *69*, 2321.  
(16) Rice, A.; Jin, Y.; Ma, X. F.; Zhang, X. C.; Bliss, D.; Larkin, J.; Alexander, M. *Appl. Phys. Lett.* **1994**, *64*, 1324.  
(17) Wu, Q.; Litz, M.; Zhang, X. C. *Appl. Phys. Lett.* **1996**, *68*, 2924.  
(18) Johnson, K. W.; Rabolt, J. F. *J. Chem. Phys.* **1973**, *58*, 4536.  
(19) Chantry, G. W.; Fleming, J. W.; Nicol, E. A.; Willis, H. A.; Cudby, M. E. A. *Chem. Phys. Lett.* **1972**, *16*, 141.  
(20) Duvillaret, L.; Garet, F.; Coutaz, J.-L. *IEEE J. Sel. Top. Quantum Electron.* **1996**, *2*, 739.  
(21) Delley, B. *J. Chem. Phys.* **1990**, *92*, 508.  
(22) Delley, B. *J. Chem. Phys.* **2000**, *113*, 7756.  
(23) Becke, A. D. *Phys. Rev. A: At., Mol., Opt. Phys.* **1988**, *38*, 3098.  
(24) Lee, C.; Yang, W.; Parr, R. G. *Phys. Rev. B: Condens. Matter Phys.* **1988**, *37*, 785.  
(25) Tsuneda, T.; Suzumura, T.; Hirao, K. *J. Chem. Phys.* **1999**, *110*, 10664.  
(26) Perdew, J. P.; Chevary, J. A.; Vosko, S. H.; Jackson, K. A.; Pederson, M. R.; Singh, D. J.; Fiolhais, C. *Phys. Rev. B: Condens. Matter Mater. Phys.* **1992**, *46*, 6671.  
(27) Boese, A. D.; Handy, N. C. *J. Chem. Phys.* **2001**, *114*, 5497.  
(28) Perdew, J. P.; Yue, W. *Phys. Rev. B: Condens. Matter Mater. Phys.* **1986**, *33*, 8800.  
(29) Perdew, J. P.; Burke, K.; Ernzerhof, M. *Phys. Rev. Lett.* **1996**, *77*, 3865.  
(30) Perdew, J. P.; Burke, K.; Ernzerhof, M. *Phys. Rev. Lett.* **1997**, *78*, 1396.  
(31) Hammer, B.; Hansen, L. B.; Norskov, J. K. *Phys. Rev. B: Condens. Matter Mater. Phys.* **1999**, *59*, 7413.  
(32) Vosko, S. H.; Wilk, L.; Nusair, M. *Can. J. Phys.* **1980**, *58*, 1200.  
(33) Hakey, P.; Ouellette, W.; Zubietta, J.; Korter, T. *Acta Crystallogr., Sect. E: Struct. Rep. Online* **2008**, *64*, o940.  
(34) Allis, D. G.; Korter, T. M. *ChemPhysChem* **2006**, *7*, 2398.  
(35) Allis, D. G.; Prokhorova, D. A.; Korter, T. M. *J. Phys. Chem. A* **2006**, *110*, 1951.  
(36) Laman, N.; Harsha, S. S.; Grischkowsky, D.; Melinger, J. S. *Opt. Express* **2008**, *16*, 4094.  
(37) Walther, M.; Plochocka, P.; Fischer, B.; Helm, H.; Jepsen, P. U. *Biopolymers* **2002**, *61*, 310.  
(38) Allis, D. G.; Hakey, P. M.; Korter, T. M. *Chem. Phys. Lett.* **2008**, *463*, 353.  
(39) *NanoEngineer-1*, 1.1.1 ed.; Nanorex, Inc.: Bloomfield Hills, MI, 2008.  
(40) *POV-Ray: Persistence of Vision Raytracer Program*, 3.6 ed.; Persistence of Vision Raytracer Pty. Ltd.: Victoria, Australia, 2004.

JP810255E